Multiscale Prediction of Viscoelastic Properties of Asphalt Concrete

Elisabeth Aigner[1]; Roman Lackner[2]; and Christian Pichler[3]

Abstract: The low viscosity of asphalt concrete at $T>135°C$ is necessary for the construction and compaction process of high-quality asphalt concrete layers. Whereas the continuous increase of viscosity with decreasing temperature is desirable for the reduction of permanent deformations during warm periods, so-called top-down cracking may occur in the course of temperature drops during cold periods. In order to explain the complex viscoelastic properties of asphalt concrete, a multiscale model is proposed. Hereby, the viscoelastic behavior of bitumen serves as input and the effect of air voids and aggregates is investigated. The viscous properties of bitumen are identified, using the bending-beam rheometer and the dynamic-shear rheometer, providing access to the viscoelastic material response for different temperature and loading regimes. With the rheological properties of bitumen at hand, the viscoelastic properties of mastic, mortar, and asphalt concrete are determined using continuum micromechanics, employing the elastic-viscoelastic "correspondence principle." The creep properties of asphalt concrete obtained from the presented mode of upscaling from the bitumen to the *asphalt* scale is validated by means of cyclic tests and static uniaxial creep tests.

DOI: 10.1061/(ASCE)0899-1561(2009)21:12(771)

CE Database subject headings: Bitumen; Asphalts; Concrete; Material properties; Micromechanics; Creep; Viscoelasticity; Predictions.

Motivation

Since the recent enlargement of the European Union (EU) in 2004, Austria is surrounded by member states of the EU. As a consequence of the single market program of the EU, in addition to north-south transit between Germany and Italy, a pronounced increase of east-west transit is already observed and expected to increase further. The increased loading of the Austrian road infrastructure by the number of vehicles, on the one hand, as well as the increased loading by the use of so-called single tires, requires (1) a rigorous assessment of the existing road infrastructure and (2) the reliable performance prediction for future projects. So far, however, this assessment is performed exclusively by means of empirical methods and/or experiments.

As a remedy, numerical analysis tools (already employed in structural engineering and soil mechanics) represent a promising alternative for the assessment of pavements. In contrast to material models already adopted for the simulation of pavement structures [see, e.g., Huet (1963); Sayegh (1965); Olard (2003)], the incorporation of finer-scale information is proposed in this paper, taking into account

- The large variability of asphalt concrete mixes, resulting from different mix designs, different constituents (e.g., bitumen, filler, aggregate, etc.), and the allowance of additives.
- Changing material behavior in consequence of thermal, chemical, and mechanical loading.

According to Blab et al. (2004), four additional observation scales may be introduced below the macroscale (see Fig. 1). Changes in the material behavior in consequence of thermal, chemical, and mechanical loading can be considered at the respective scale of observation and, via upscaling, their effect on the macroscopic material behavior is obtained. Within this paper, upscaling of viscoelastic properties from the bitumen to the macroscale is presented, allowing us to relate the rheological behavior of asphalt concrete to the behavior of bitumen, i.e., the only constituent in asphalt concrete exhibiting viscoelastic behavior.

In the following section, the theoretical basis for upscaling of creep properties within continuum micromechanics using the elastic-viscoelastic correspondence principle is presented. Thereafter, rheological properties of bitumen, serving as input for the proposed multiscale model, are identified experimentally. Finally, the performance of the proposed upscaling scheme is assessed by means of testing of mastic, mortar, and asphalt concrete experiments, considering four different types of asphalt concrete.

Upscaling of Creep Properties

Recent developments in the finer-scale characterization of materials provide the basis for the development of so-called "bottom-up" multiscale models by relating the macroscopic material behavior to finer-scale properties of the material. After identification of the material properties at the finer scales, upscaling techniques are used to shift the finer-scale information from an

[1]Research Assistant, Christian-Doppler-Laboratory for "Performance-based Optimization of Flexible Pavements," Institute for Mechanics of Materials and Structures, Vienna Univ. of Technology, Karlsplatz 13/202, A-1040 Vienna, Austria. E-mail: Elisabeth.Aigner@tuwien.ac.at

[2]Professor, Material Technology Innsbruck, Univ. of Innsbruck, Technikerstraße 13, A-6020 Innsbruck, Austria (corresponding author). E-mail: roman.lackner@uibk.ac.at

[3]University Assistant, Material Technology Innsbruck, Univ. of Innsbruck, Technikerstraße 13, A-6020 Innsbruck, Austria. E-mail: Christian.Pickler@uibk.ac.at

Note. This manuscript was submitted on October 9, 2007; approved on June 3, 2009; published online on November 13, 2009. Discussion period open until May 1, 2010; separate discussions must be submitted for individual papers. This paper is part of the ***Journal of Materials in Civil Engineering***, Vol. 21, No. 12, December 1, 2009. ©ASCE, ISSN 0899-1561/2009/12-771–780/$25.00.

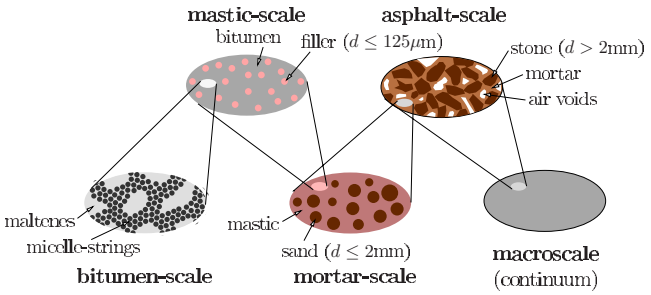

Fig. 1. Multiscale model with four additional observation scales below the macroscale

observation scale to the next-higher one, considering the respective composite microstructure. Depending on the encountered material microstructure, two modes of upscaling can be distinguished:

1. The unit-cell approach for periodically arranged microstructures.
2. The representative-volume-element (RVE) approach for microstructures with randomly arranged inclusions.

For upscaling of properties of asphalt concrete, showing a randomly arranged microstructure, the RVE approach is appropriate. In this context, use of continuum micromechanics is proposed in this paper for upscaling of elastic and viscoelastic properties of asphalt concrete.

Homogenization of Elastic Properties: Continuum Micromechanics

Continuum micromechanics is an analytical technique for determination of the effective behavior of composites, taking the arrangement and properties of the material phases into account. The constitutive law for the rth material phase at the position $\mathbf{x}$ is given by

$$\boldsymbol{\sigma}_r(\mathbf{x}) = \mathbf{c}_r : \boldsymbol{\varepsilon}_r(\mathbf{x}) \tag{1}$$

Within continuum micromechanics, a localization tensor $\mathbf{A}$ is introduced, relating the homogenized strain tensor $\mathbf{E}$ to the local strain tensor $\boldsymbol{\varepsilon}$ at $\mathbf{x}$

$$\boldsymbol{\varepsilon}(\mathbf{x}) = \mathbf{A}(\mathbf{x}) : \mathbf{E} \tag{2}$$

with

$$\mathbf{E} = \langle \boldsymbol{\varepsilon}(\mathbf{x}) \rangle_V = \frac{1}{V} \int_V \boldsymbol{\varepsilon}(\mathbf{x}) dV \tag{3}$$

The homogenized stress tensor Σ is obtained from volume averaging of the local stress tensor $\boldsymbol{\sigma}(\mathbf{x})$, reading

$$\Sigma = \langle \boldsymbol{\sigma}(\mathbf{x}) \rangle_V = \frac{1}{V} \int_V \boldsymbol{\sigma}(\mathbf{x}) dV \tag{4}$$

Considering Eqs. (1) and (2) in Eq. (4) and comparing the so-obtained result with the macroscopic stress-strain law

$$\Sigma = \mathbf{C}_{\text{eff}} : \mathbf{E} \tag{5}$$

leads to the effective material tensor $\mathbf{C}_{\text{eff}}$ as

$$\mathbf{C}_{\text{eff}} = \langle \mathbf{c} : \mathbf{A} \rangle_V \tag{6}$$

When considering an idealized microstructure, the unknown localization tensor $\mathbf{A}$ can be estimated. For a microstructure showing a clear matrix-inclusion morphology, the Mori-Tanaka scheme (Mori and Tanaka 1973) is used. Hereby, the localization tensor for Ith inclusion is given by

$$\mathbf{A}_I = [\mathbf{I} + \mathbf{S}_I : (\mathbf{c}_M^{-1} : \mathbf{c}_I - \mathbf{I})]^{-1} : \{f_M \mathbf{I} + f_I [\mathbf{I} + \mathbf{S}_I : (\mathbf{c}_M^{-1} : \mathbf{c}_I - \mathbf{I})]^{-1}\}^{-1} \tag{7}$$

where the indices I and M refer to the inclusion and matrix phase, respectively. In Eq. (7), f_I and f_M represent the volume fraction of the inclusions and the matrix, respectively, and $\mathbf{S}$ denotes the so-called fourth-order Eshelby tensor. From $\langle \mathbf{A} \rangle_V = \mathbf{I}$, $\langle \mathbf{A} \rangle_{V_M}$ is obtained as

$$\langle \mathbf{A} \rangle_{V_M} = \frac{1}{f_M} (\mathbf{I} - f_I \mathbf{A}_I) \tag{8}$$

Considering Eqs. (7) and (8) in Eq. (6), the effective shear modulus μ_{eff} is obtained for the case of spherical inclusions as

$$\mu_{\text{eff}} = \frac{f_M \mu_M + f_I \mu_I [1 + \beta(\mu_I/\mu_M - 1)]^{-1}}{f_M + f_I [1 + \beta(\mu_I/\mu_M - 1)]^{-1}} \tag{9}$$

where μ_I and μ_M denote the shear moduli of the inclusions and the matrix, respectively. $\beta = 6(k_M + 2\mu_M)/[5(3k_M + 4\mu_M)]$, with k_M as the bulk modulus of the matrix material.

Homogenization of Viscoelastic Properties: Elastic-Viscoelastic Correspondence Principle

Viscoelasticity is used to describe the behavior of materials showing an accumulation of strains under constant stress (creep) and/or a reduction of stress under constant strain (relaxation). Depending on the prescribed quantity (strain or stress), the respective unknown quantity (stress or strain) is determined, using the relaxation modulus $E(t) = \sigma(t)/\varepsilon_0$ and the creep compliance $J(t) = \varepsilon(t)/\sigma_0$, respectively. For example, for a specified stress history $\sigma(t)$, the strain at time instant t reads

$$\varepsilon(t) = \int_0^t J(t - \tau) \frac{\partial \sigma(\tau)}{\partial \tau} d\tau \tag{10}$$

Applying the Laplace-Carson transformation

$$\mathcal{LC}[f(t)] = f^*(p) = p \int_0^\infty f(t) e^{-pt} dt \tag{11}$$

with p as the complex variable, and $f^*(p) = p\hat{f}(p)$, to Eq. (10), one gets

$$\varepsilon^*(p) = J^*(p) \sigma^*(p) \tag{12}$$

The analogy between Eq. (12) and the linear-elastic constitutive law is the basis for the solution of viscoelastic problems within the correspondence principle (see, e.g., Mandel 1966). Hereby, the material parameters in the solution of the respective elastic problem are replaced by the respective Laplace-Carson transformed viscoelastic parameters. For example, the elastic shear compliance $1/\mu$ is replaced by the Laplace-Carson transformed creep-compliance function for deviatoric creep, $J^*_{\text{dev}}(p)$. Inverse Laplace-Carson transformation

$$\mathcal{LC}^{-1}[f^*(p)] = f(t) = \frac{1}{2i\pi} \int_\Gamma \frac{f^*(p)}{p} e^{pt} dp \tag{13}$$

where Γ is parallel to the imaginary axis having all poles of $f^*(p)$ on the left, delivers the corresponding solution in the time domain. Fig. 2 contains the creep compliance $J(t)$ and the Laplace-

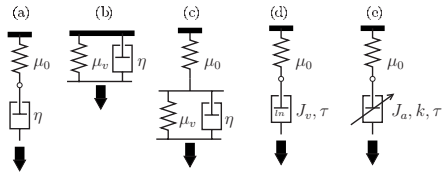

rheological model	creep compliance function $J(t)$	Laplace-Carson transform $J^*(p)$
(a) Maxwell	$J(t)=\frac{1}{\mu_0}+\frac{1}{\eta}t$	$J^*(p)=\frac{1}{\mu_0}+\frac{1}{\eta}\frac{1}{p}$
(b) Kelvin-Voigt	$J(t)=\frac{1}{\mu_v}\left(1-e^{-\mu_v t/\eta}\right)$	$J^*(p)=\frac{1}{\mu_v+\eta p}$
(c) 3-parameter	$J(t)=\frac{1}{\mu_0}+\frac{1}{\mu_v}\left(1-e^{-\mu_v t/\eta}\right)$	$J^*(p)=\frac{1}{\mu_0}+\frac{1}{\mu_v+\eta p}$
(d) logarithmic	$J(t)=\frac{1}{\mu_0}+J_v \ln\left(1+\frac{t}{\bar{\tau}}\right)$	$J^*(p)=\frac{1}{\mu_0}+J_v e^{p\bar{\tau}}\Gamma[0,p\bar{\tau}]$
(e) Power-law	$J(t)=\frac{1}{\mu_0}+J_a\left(\frac{t}{\bar{\tau}}\right)^k$	$J^*(p)=\frac{1}{\mu_0}+J_a\left(\frac{1}{p\bar{\tau}}\right)^k\Gamma[k+1]$

Fig. 2. Rheological models, model parameters for the description of deviatoric creep, creep compliance, and Laplace Carson transform: (a) Maxwell model; (b) Kelvin-Voigt model; (c) three-parameter model; (d) spring with logarithmic dash pot; and (e) PL model

Carson transform $J^*(p)$ for different rheological models. With the elastic solution for the effective properties of composite materials at hand [Eq. (9)], the correspondence principle gives access to the effective (homogenized) creep compliance of a matrix/inclusion composite as

$$J^*_{\text{eff}}(p)=\frac{f_M+f_I[1+\beta^*(J^*_M/J^*_I-1)]^{-1}}{f_M/J^*_M+f_I/J^*_I[1+\beta^*(J^*_M/J^*_I-1)]^{-1}} \tag{14}$$

with $\beta^*=6(k^*_M+2/J^*_M)/[5(3k^*_M+4/J^*_M)]$. For the case of deviatoric creep of the matrix and elastic behavior of the inclusions, $k^*_M=k_M$ and $1/J^*_1=\mu_I$. Application of the inverse Laplace-Carson transformation

$$J_{\text{eff}}(t)=\mathcal{LC}^{-1}[J^*_{\text{eff}}(p)] \tag{15}$$

leads to the effective creep compliance of the composite material in the time domain. Whereas the inverse transformation can be performed analytically for simple rheological models, numerical techniques [employing, e.g., the Gaver-Stehfest algorithm (Stehfest 1970)] are needed for material phases showing a complex rheological behavior. Hereby, the transformation provides discrete points of the effective creep-compliance function $J_{\text{eff}}(t)$. Approximation of $J_{\text{eff}}(t_i)$ by a creep-compliance function affine to the rheological behavior of the material phases exhibiting time-dependent behavior gives access to the effective viscoelastic model parameters (Ewers and Heukelom 1964).

Identification of Rheological Properties of Bitumen

In this section, the viscous properties of bitumen, serving as input for the proposed multiscale model, are identified using two types of experiments: the bending-beam rheometer (BBR) test (SHRP-A-370 1994) in the low-temperature regime ($-30<T<0\,^\circ$C) and the dynamic-shear rheometer (DSR) test (SHRP-A-370 1994) in the elevated temperature regime ($0<T<80\,^\circ$C). In the experimental program, the following three types of bitumen were considered:

- A bitumen B70/100 with a penetration at 25°C between 70 and 100;
- A bitumen B50/70 with a penetration at 25°C between 50 and 70; and

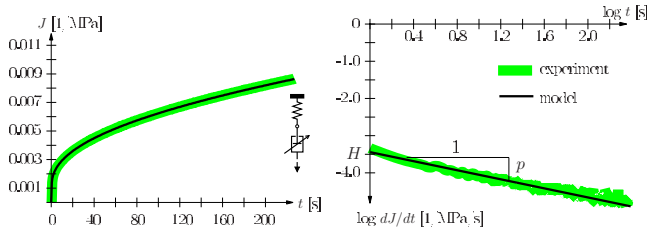

Fig. 3. Comparison of model response with experimental data from BBR: (a) creep compliance; (b) creep-compliance rate for the determination of temperature-dependent creep parameters

- A polymer modified bitumen B45/80 with a penetration at 25°C between 45 and 80.

BBR

The BBR is a three-point bending-beam experimental setup, designed to characterize the low-temperature viscous behavior of bitumen. A load of $F=980$ mN is applied at the midspan of the beam specimen ($125\times12.5\times6.25$ mm) for 240 s. The creep compliance J (MPa^{-1}) is obtained in the form

$$J(t)=\frac{\varepsilon(t)}{\sigma}=\frac{4bh^3}{Fl^3}u(t) \tag{16}$$

where $\varepsilon(t)=6h/l^2\times u(t)$ with $u(t)$ as the monitored midspan deflection. In case of bitumen, the experimental results are well described by the so-called power-law (PL) model [Fig. 3(a)], with the creep compliance reading

$$J(t)=\frac{1}{\mu_0}+J_a\left(\frac{t}{\bar{\tau}}\right)^k \tag{17}$$

In Eq. (17), μ_0 (MPa) is the shear modulus and J_a (MPa^{-1}) is the viscous part of the creep compliance at $t=\bar{\tau}$. For the characterization of the model parameters, the creep-compliance rate dJ/dt is used [see Fig. 3(b)], with

$$dJ/dt=\frac{J_a k}{\bar{\tau}}\left(\frac{t}{\bar{\tau}}\right)^{k-1}=H\left(\frac{t}{\bar{\tau}}\right)^p \tag{18}$$

where H ($\text{MPa}^{-1}\,\text{s}^{-1}$) represents the creep-compliance rate at $t=\bar{\tau}$ and p (−)=slope of the linear model response in the $\log dJ/dt$-$\log t$ diagram (see Fig. 3). The temperature-dependent model parameters H and p are determined from regression analysis. The values for the parameters p and H, identified at five different temperatures (−24, −18, −12, −6, and 0°C), give access to the temperature dependence of the model parameter p, with

$$p(T)=p_0+c(T-\bar{T}) \tag{19}$$

where T=actual temperature and $\bar{T}$=reference temperature. The temperature dependence of the model parameter H, on the other hand, is described by the Arrhenius-type law

$$H(T)=H_0\exp\left[\frac{-E_a}{R}\left(\frac{1}{T}-\frac{1}{\bar{T}}\right)\right] \tag{20}$$

Hereby, H_0=creep-compliance rate at $t=\bar{\tau}$ for $T=\bar{T}$; E_a (J/mol)=activation energy; and R=gas constant. For the considered types of bitumen, the parameters describing the temperature dependence of the model parameters p and H are given in Table 1.

Table 1. Model Parameters for Considered Types of Bitumen Obtained from BBR and DSR Tests (Reference Temperature $T=-12\,^{\circ}\mathrm{C}$)

Bitumen	H_0 (mm/m/MPa/s)	p_0 (−)	c (−)	E_a/R (K)
B70/100	0.376	−0.41	0.01	9,500
pmB45/80	0.611	−0.46	0.011	8,600
B50/70	0.254	−0.51	0.013	10,600

DSR

Whereas H and p can be determined from BBR tests, the DSR equipment "Haake Mars" (temperature range: − 40 to 150°C; frequency range: 100 to 10^{-5} Hz) is used to characterize the temperature-independent model parameter μ_0. Hereby, a bitumen film with $d/h=25$ mm/1 mm for high temperatures and $d/h=8$ mm/2 mm for low temperatures is placed between a lower fixed plate and an upper oscillating plate undergoing a temperature and frequency sweep from − 20 to +46°C and 0.1 to 50 Hz, respectively.

The delivered phase angle φ and the complex shear modulus μ^* are related to the relaxation function via the Laplace-Carson transformation (see Appendix). Based on the values of μ^* and φ, the storage and loss modulus are determined: $\mu'=\mathrm{Re}(\mu^*)=\mu^*\cos\varphi$ and $\mu''=\mathrm{Im}(\mu^*)=\mu^*\sin\varphi$. The experimentally obtained values for μ' and μ'' are plotted in the so-called Cole-Cole diagram (see Fig. 4). The temperature-independent model parameter of the PL model μ_0 is obtained from curve fitting, aiming at the best fit between the analytical calculated model response (see Appendix) and the experimental data in the Cole-Cole diagram. This approach is illustrated in Fig. 4 for B50/70 and pmB45/80.

Upscaling of Viscoelastic Properties and Validation

Bitumen-Filler Interaction at the Filler Scale

With the input parameters $p(f_f=0\,\%)$ and $H(f_f=0\,\%)$ and, thus, k and J_a for pure bitumen at hand, Eq. (14) is used to predict the creep parameters for different bitumen-filler composites, referred to as mastic. Hereby, the matrix material (bitumen) is associated with viscoelastic behavior, whereas elastic behavior is assigned to the inclusion phase (filler). According to the correspondence principle, the Laplace-Carson transform of the deviatoric creep compliance of the bitumen matrix reads (see Table 1)

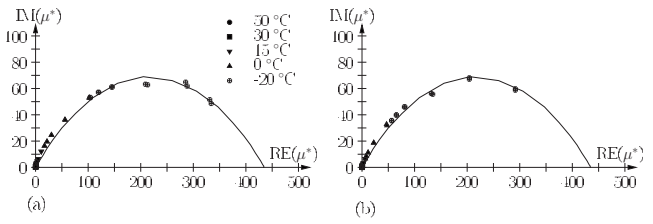

Fig. 4. DSR experimental results and model response (solid line) for (a) bitumen B50/70 (model parameters: $1/\mu_0=0.0023$ MPa^{-1}, $J_a=0.0015$ MPa^{-1}, $k=0.39$, and $\bar{\tau}=1$ s; (b) bitumen B45/80 (model parameters: $1/\mu_0=0.0023$ MPa^{-1}, $J_a=0.0014$ MPa^{-1}, $k=0.38$, and $\bar{\tau}=1$ s)

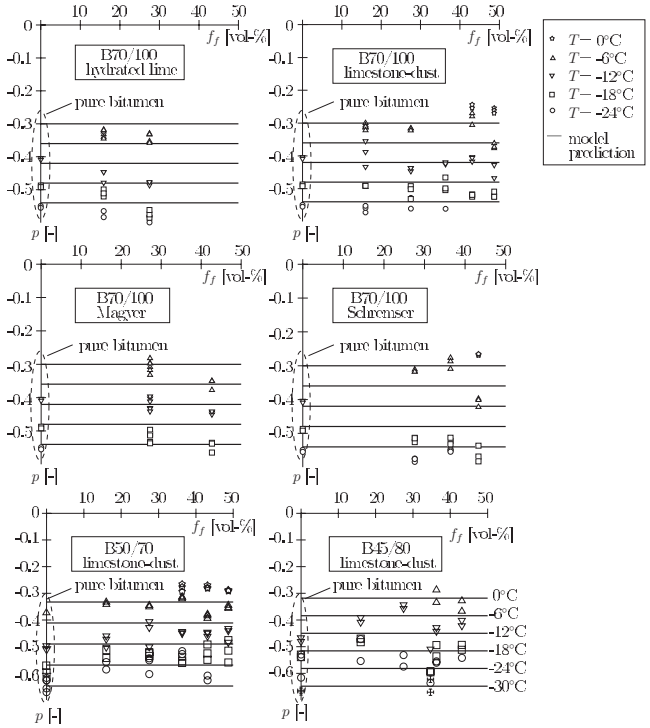

Fig. 5. Experimental results for p and model prediction for mastic consisting of B70/100 and four different types of filler and for mastic consisting of B50/70 and B45/80 with limestone dust

$$J_b^*(p)=\frac{1}{\mu_0}+J_a\left(\frac{1}{p\bar{\tau}}\right)^k\Gamma[k+1] \tag{21}$$

Under hydrostatic loading, bitumen is assumed to behave elastically, giving the Laplace-Carson transform of the bulk modulus as $k_b^*=k_b$. Inserting Eq. (21), $k_b^*=k_b$, and $1/J_f^*=\mu_f$ for the filler into Eq. (14) and performing the inverse Laplace-Carson transformation give access to the effective creep compliance $J_{\mathrm{eff}}(t)$ and, thus, to the effective creep parameters H_{eff} and p_{eff} for the mastic.

In order to verify the predicted values of H_{eff} and p_{eff}, additional BBR experiments were conducted on mastic with B70/100 with four types of filler, and B50/70 and B45/80 with limestone dust as filler (see Figs. 5 and 6). The effective creep parameters shown from Figs. 5 and 6 are computed by replacing the filler content f_f in Eq. (14) by the *effective* volume content of the filler, f_{eff}, with (Lackner et al. 2004)

$$f_{\mathrm{eff}}=\frac{f_f}{1-f_a} \tag{22}$$

where f_f=volume fraction of the filler in the mastic. The volume of air voids in the case of maximum filler compaction, f_a, appearing in Eq. (22) is determined using the Ridgen filler compaction apparatus (ÖNORM-EN-1097-4 1999). These air voids, when filled with bitumen, do not introduce viscous behavior and, thus, are added to the volume fraction of the filler. In Fig. 5, a slight decrease of p is observed for increasing filler content which could not be reproduced using the upscaling scheme (upscaling gave almost no effect of the amount of filler on p). This effect may be explained by the increased material elasticity in consequence of inclusion-inclusion contact and clustering.

In order to validate the upscaling scheme at the *mastic* scale at the elevated temperature regime, DSR experiments on mastic, composed of limestone dust and B50/70 and B45/80, were con-

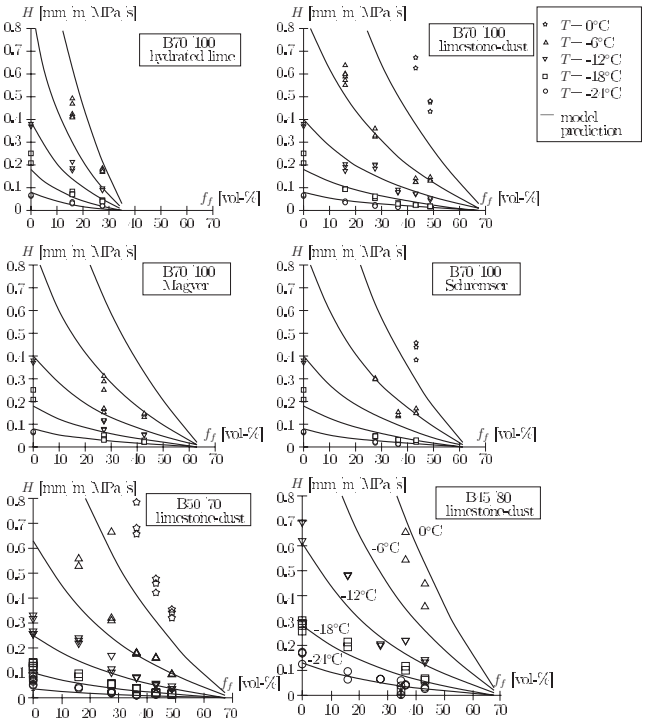

Fig. 6. Experimental results for H and model prediction for mastic consisting of B70/100 and four different types of filler and for mastic consisting of B50/70 and B45/80 with limestone dust

ducted. Hereby, a bitumen/filler ratio of 1:1.9 for B50/70 and a bitumen/filler ratio of 1:1.4 for B45/80 were chosen. With the input parameters for bitumen at hand (see Fig. 4), Eq. (14) is used for the prediction of the model parameters for mastic. Again, the matrix material (bitumen) is associated with viscoelastic behavior, whereas elastic behavior is assigned to the filler. Similar to upscaling in the low-temperature regime (BBR experiments), the filler content f_f was replaced by the effective filler content f_{eff} for determination of the effective creep compliance of mastic. Fig. 7 shows the experimental results for B50/70 and B45/80 with limestone dust and the respective viscoelastic model using the parameters obtained from upscaling, fitting well the experimentally obtained results. It is noteworthy that the effect of the model parameter J_a on the model response in the Cole-Cole diagram is rather small. Thus, only the elastic parameter $1/\mu_0$ and k, on the one hand, can be identified for pure bitumen, and the effective

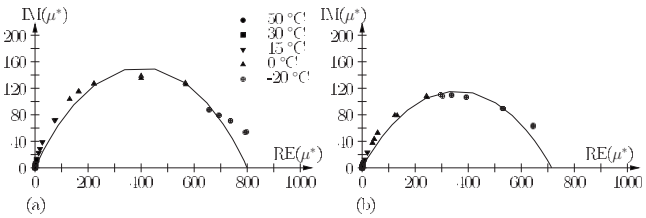

Fig. 7. DSR results and model response for (a) mastic with bitumen B50/70 and limestone dust (bitumen/filler ratio=1:1.9; model parameters from upscaling: $1/\mu_{0,\text{eff}}=0.001\,25$ MPa^{-1}, $J_{a,\text{eff}}=0.0015$ MPa^{-1}, $k_{\text{eff}}=0.41$, and $\bar{\tau}=1$ s); (b) mastic with bitumen B45/80 and limestone dust (bitumen/filler ratio=1:1.4; model parameters from upscaling: $1/\mu_{0,\text{eff}}=0.0014$ MPa^{-1}, $J_{a,\text{eff}}=0.0014$ MPa^{-1}, $k_{\text{eff}}=0.40$, and $\bar{\tau}=1$ s)

Table 2. Type of Filler Considered in the Experimental Program and Respective Filler Properties

Type of filler	Real mass density (kg/m^3)	Air voids[a] f_a (vol %)	Specific surface (m^2/kg)
Hydrated lime	2,230	64.0	15,800
Limestone dust	2,710	30.5	2,050
Magyer	2,760	35.2	4,990
Schremser	2,700	37.1	2,580

[a]Air voids in case of maximum densification (ÖNORM-EN-1097-4 1999).

model parameters $1/\mu_{\text{eff}}$ and k_{eff} obtained from upscaling, on the other hand, can be validated by DSR testing of mastic.

Matrix-Aggregate Interaction at the Higher Scales

In order to validate the model parameters for mortar and asphalt concrete obtained from upscaling, static creep tests are used for determination of parameters representing the long-term response, and cyclic tests are performed at different frequency and temperature regimes in order to assess the predictive capability of the multiscale model as regards elastic and short-term viscous properties. The considered types of asphalt concrete, their properties, and the mix design are given in Tables 2 and 3. In the following subsection, results obtained from static experiments are presented and compared with viscoelastic model parameters obtained from upscaling, using Eqs. (14) and (15).

Static Tests

Both $J_{a,\text{eff}}$ and k_{eff} obtained from upscaling, describing the long-term response of the material, are validated by static uniaxial creep tests using prismatic asphalt concrete specimen with a cross-section of 50 mm × 50 mm for testing of SMA11 and of 60 mm × 60 mm for testing of BT22. Within the conducted experimental program, the applied load was set equal to 10% of the tensile strength at the respective testing temperature. The experimentally obtained creep compliance is given by

$$J = \varepsilon(t)/\sigma_0 \tag{23}$$

where σ_0=applied (constant) tensile stress and $\varepsilon(t)$=monitored strain history. For the prediction of the creep behavior using the multiscale model, the values for p and H for the respective types of bitumen are given in Table 1. Hereby, the temperature dependence of the model parameters p and H is considered according to Eqs. (19) and (20). With the input parameters given in Table 1 at hand, Eq. (14) is used to predict the creep parameters for the considered types of asphalt concrete. Hereby, upscaling is performed in a stepwise manner, following the multiscale model shown in Fig. 1. Thus, only bitumen and filler are considered in the first step. In the second step, this bitumen-filler composite (mastic) becomes the new matrix material where additional aggregates, ranging from 0 to 4 mm, are added. In the third step, aggregates, ranging from 4 to 22 mm, and air voids are added into this new matrix material. When considering two types of inclusions (e.g., aggregate and air within the third step), Eq. (14) is extended as

Table 3. Types of Asphalt Concrete Considered in Experimental Program

Asphalt type	SMA11-B70/100-D	SMA11-B45/80-D	BT22-B50/70-H	BT22-B45/80-H
Bitumen	B70/100	B45/80	B50/70	B45/80
Additive	Viatop premium	Viatop premium	—	—
Filler	Limestone dust	Limestone dust	Limestone dust	Limestone dust
Aggregate	Diabas	Diabas	Hollitzer	Hollitzer

$$J^*_{\text{eff}} = \frac{f_M + f_s\left[1+\beta^*\left(\frac{J^*_M}{J^*_n}-1\right)\right]^{-1} + f_a\left[1+\beta^*\left(\frac{J^*_M}{J^*_a}-1\right)\right]^{-1}}{f_M/J^*_M + f_s/J^*_s\left[1+\beta^*\left(\frac{J^*_M}{J^*_s}-1\right)\right]^{-1} + f_a/J^*_a\left[1+\beta^*\left(\frac{J^*_M}{J^*_a}-1\right)\right]^{-1}} \tag{24}$$

with $\beta^*=6(k^*_M+2/J^*_M)/[5(3k^*_M+4/J^*_M)]$ and the indices M, s, and a referring to the matrix, the stone, and the air phase, respectively.

For all three upscaling steps, the matrix material is associated with viscoelastic behavior described by the PL model (see Table 1), whereas elastic behavior is assigned to the inclusions. Under hydrostatic loading, the matrix is assumed to behave elastically, giving $k^*_M=k_M$. Inserting the Laplace-Carson transformed creep compliance, $k^*_M=k_M$, $1/J^*_s=\mu_s=2\times10^5$ MPa^{-1} (Holl 1971), and $1/J^*_a=\mu_a=0$ into Eqs. (14) and (24), respectively, and performing the inverse Laplace-Carson transformation give access to the effective creep compliance $J_{\text{eff}}(t)$ and, thus, to the effective creep parameters $J_{a,\text{eff}}$ and k_{eff} of asphalt concrete. Hereby, upscaling was performed using (1) the original; (2) the effective filler content according to Eq. (22); and (3) in addition to the effective filler content the effective stone content. As regards determination of the latter, the maximum compaction was determined according to DIN-18126 (1996). The required content of air voids for limestone-dust filler at maximum compaction is given in Table 4. The content of air voids for the Diabas and the Hollitzer aggregate mixture at maximum compaction was obtained as 25 and 15%, respectively.

The results obtained from upscaling from the bitumen scale to the macroscale are depicted in Fig. 8 and compared with the respective values obtained from the uniaxial creep experiments. The so-obtained temperature dependence of the creep parameters H and p captures well the experimentally obtained results for asphalt concrete. The activation energy at the macroscale remains unchanged during scale transition from the bitumen scale to the macroscale.

Consideration of the effective filler content in the upscaling procedure leads to a shift of the model parameters obtained from upscaling toward less viscous and more pronounced elastic response, yielding a better agreement between model prediction and experimental results. After the introduction of the effective stone content in addition to the effective filler content for the mastic, the experimentally obtained results for H are well captured by the multiscale model. As regards upscaling of the model parameter p, the observed deviation from the experimental results may be explained by the use of the Mori-Tanaka scheme, neglecting contact between particles. Consideration of contact between the particles would increase the elastic material response, thus resulting in a reduction of the parameter p.

Fig. 9 gives the value for H for the different upscaling steps at two temperatures (-10 and 20°C) for the types of asphalt concrete given in Table 2. The initial (input) value of H for bitumen is compared with the respective values obtained for mastic, mortar, and asphalt concrete. The difference in the decrease of H by addition of filler, sand, and stone for SMA11-B70/100-D and SMA11-B45/80-D, on the one hand, and BT22-B50/70-H and BT22-B45/80-H, on the other hand, is explained by the rather low filler content considered in the two BT22 mixtures. However, the low filler content of the mix design is compensated in the next upscaling step, considering the rather high eigenfiller content present in the aggregate fraction from 0 to 4 mm.

Table 4. Composition of Types of Asphalt Concrete Considered in Experimental Program

Asphalt type	Bitumen (vol %)	Filler (vol %)	Aggregate 0–4 mm (vol %)	Aggregate 4–22 mm (vol %)	Air (vol %)
SMA11-B70/100-D	15.7	3.7	23.1	54.4	3.1
SMA11-B45/80-D	15.5	3.7	22.9	54.1	3.7
BT22-B50/70-H	11.1	0.4	33.3	49.9	5.2
BT22-B45/80-H	11.1	0.4	33.4	50.2	4.8

Cyclic Tests

Cyclic tests are performed at different temperatures (ranging from -15 to 30°C) and different frequencies, ranging from 0.1 to

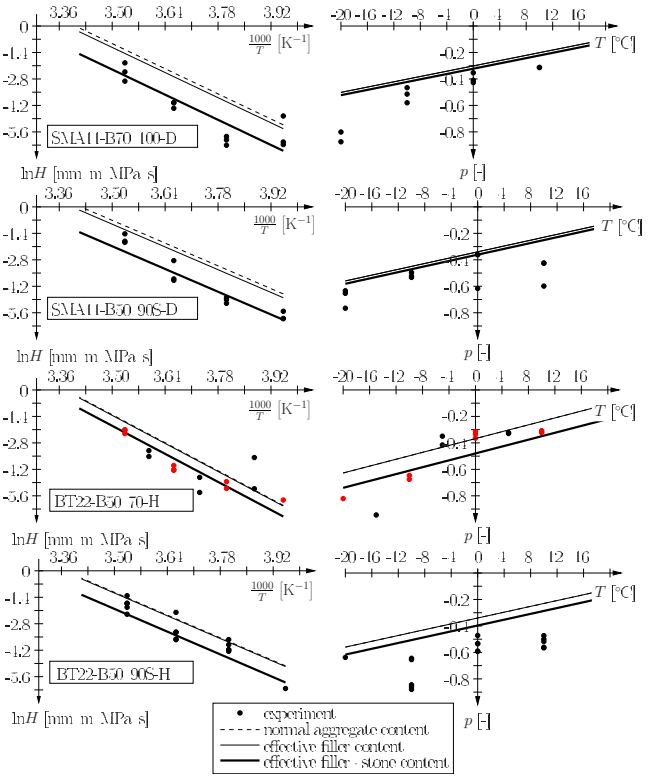

Fig. 8. Experimental results for H and p and multiscale prediction for SMA11-B70/100-D, SMA11-B45/80-D, BT22-B50/70-H, and BT22-B45/80-H

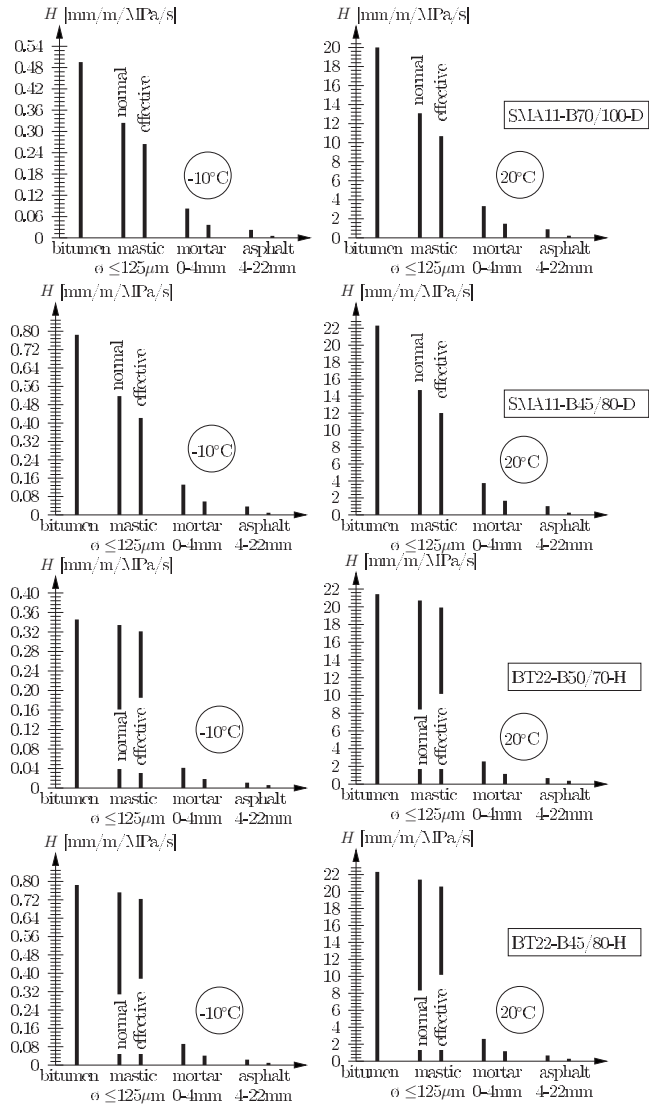

Fig. 9. Decrease of H by the allowance of aggregates obtained from upscaling for $T=-10°C$ and $T=20°C$

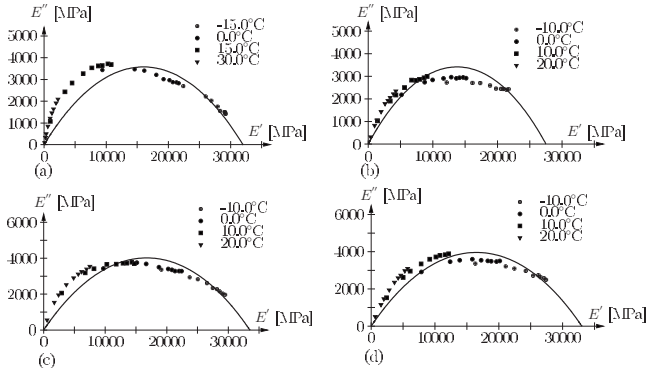

Fig. 10. Experimental results from cyclic tests and multiscale prediction for asphalt concrete (a) SMA11-70/100-D (model parameters from upscaling: $1/E_{0,\text{eff}}=3.0\times10^{-5}$ MPa^{-1}, $J_{a,\text{eff}}=1.7\times10^{-5}$ MPa^{-1}, $k_{\text{eff}}=0.3$, and $\bar{\tau}=1$ s); (b) SMA11-45/80-D (model parameters from upscaling: $1/E_{0,\text{eff}}=3.03\times10^{-5}$ MPa^{-1}, $J_{a,\text{eff}}=3.5\times10^{-5}$ MPa^{-1}, $k_{\text{eff}}=0.3$, and $\bar{\tau}=1$ s); (c) BT22-50/70-H (model parameters from upscaling: $1/E_{0,\text{eff}}=3.125\times10^{-5}$ MPa^{-1}, $J_{a,\text{eff}}=2.93\times10^{-5}$ MPa^{-1}, $k_{\text{eff}}=0.28$, and $\bar{\tau}=1$ s); and (d) BT22-45/80-H (model parameters from upscaling: $1/E_{0,\text{eff}}=3.57\times10^{-5}$ MPa^{-1}, $J_{a,\text{eff}}=5.4\times10^{-5}$ MPa^{-1}, $k_{\text{eff}}=0.3$, and $\bar{\tau}=1$ s)

20 Hz, focusing on the short-term material response of asphalt concrete. These tests are performed either under uniaxial loading conditions using prismatic specimens or by using a bending-beam experimental setup. From the measured load (stress) and displacement (strain) history, the complex modulus E^* and the phase angle φ are determined (ÖNORM-EN-12697-26 2004). The so-obtained values for E^* and φ are plotted in the Cole-Cole diagram (see Fig. 10). Hereby, every point refers to a certain temperature-frequency pair considered in the experimental program. The experimental results are compared with the material response of asphalt concrete predicted by the multiscale model. Based on the viscoelastic properties of pure bitumen, the multiscale approach [Eq. (14) and (24)] is used to predict the creep parameters of mastic, mortar, and asphalt concrete. Again, the matrix material (at the respective scale) is associated with viscoelastic behavior, whereas elastic behavior is assigned to filler, sand, and stone.

Fig. 10 shows the experimental results for the considered types of asphalt concrete listed in Table 3 and the prediction by the multiscale model. The latter agrees well with the experimentally obtained results, especially in the low-temperature regime. The discrepancy of experimental results and model response of SMA11-70/100-D and SMA11-45/80-D is explained by the use of the PL model, well suited to describe the material response in the low-temperature regime.

Conclusions

In this paper, a multiscale model for the bottom-up prediction of the viscoelastic properties of asphalt concrete is proposed. Hereby, the thermorheological properties were assigned to the bitumen only and, via upscaling, the viscoelastic properties of mastic, mortar, and asphalt concrete were determined. The viscous behavior of bitumen was described by the so-called PL model, with the parameters J_a (initial creep compliance) and k (exponent of the nonlinear dashpot) of the PL model serving as input for the multiscale model. The viscoelastic model parameters obtained for mastic and asphalt concrete predicted by the multiscale model were compared with respective experimental data, leading to the following conclusions:

- The viscous properties of mastic obtained from BBR tests and DSR tests showed good agreement with the model parameters predicted by the multiscale model. This agreement was achieved by replacing the volume fraction for filler by the so-called effective filler content.
- The model parameters for asphalt concrete predicted by the multiscale model showed good agreement with the respective results from static tests conducted at different temperatures. This agreement was further improved by replacing the volume fractions of sand and stone by the respective effective volume fractions. Interestingly, the activation energy E_a of the Arrhenius law used to describe the temperature dependence of the model parameter H for bitumen remains unchanged during upscaling from the bitumen scale to the macroscale.
- Within the multiscale model, the addition of elastic inclusions resulted in almost no change of the parameter p. The parameter H, on the other hand, was significantly reduced during upscaling from the bitumen to the macroscale. The decrease of H was affected by the content of the different aggregate frac-

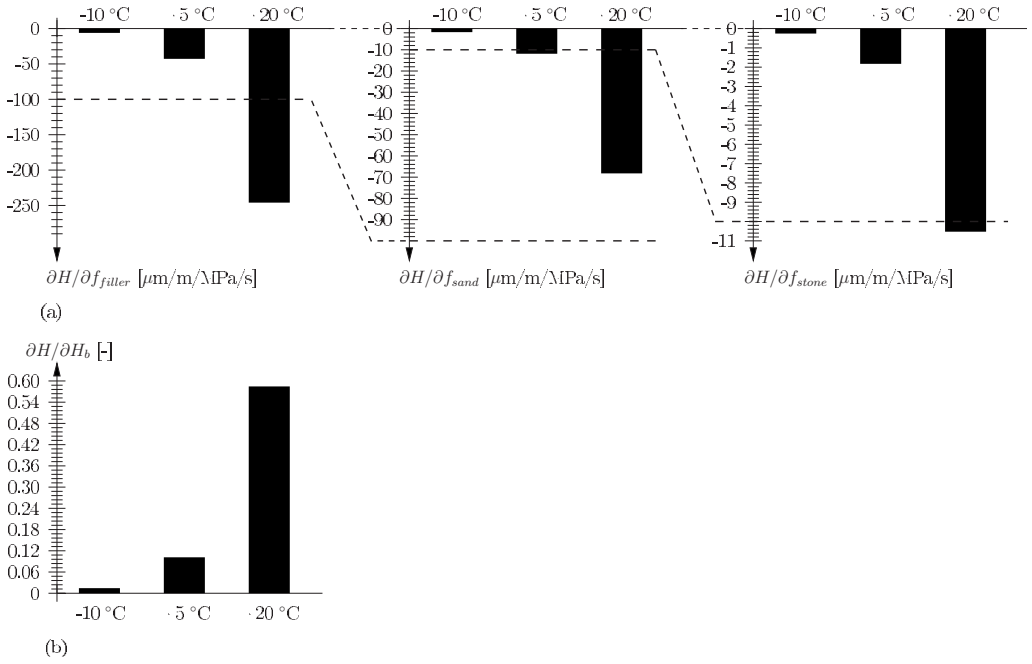

Fig. 11. Sensitivity of viscoelastic model parameter H of asphalt concrete; (a) for changes of the filler, sand, and stone fraction; (b) for changes of the viscoelastic properties of bitumen as predicted by the multiscale model

tions with eigenfiller present in the sand fraction showing a significant influence on H. Particle-particle contact may be taken into account, allowing us to reproduce the more pronounced elastic behavior, reflected by a slight decrease of p as the aggregate content increases.

By adapting the mix design, serving as input for the multiscale model, the sensitivity of the viscoelastic response of asphalt concrete with respect to certain modifications in the mix design can be determined. Fig. 11 illustrates this approach for the investigated asphalt concrete SMA11-B70/100-D, showing the sensitivity of the viscoelastic model parameter H for changes in the mix design and the bitumen characteristics. Similar as observed in previous findings, the surface/volume ratio of the aggregates defines mainly the effect of aggregates on the viscous properties of the composite. Thus, the largest impact on the viscoelastic properties of asphalt concrete was predicted by the multiscale model for changes in the filler content. The effect of changes in the bitumen characteristics on the asphalt concrete properties strongly depends on the considered temperature range, with the multiscale model predicting the largest impact in the high-temperature regime. Future work will focus on an adaptation of the Mori-Tanaka approach, considering particle-particle contact, particle shape, and chemical reactions inside asphalt concrete.

Results regarding the adaptation of the employed upscaling scheme from the Mori Tanaka scheme toward the so-called generalized self consistent scheme, suitable for highly filled matrix-inclusion type morphologies investigated in this paper, can be found in Pichler and Lackner (2009) and Pichler et al. (2009).

Acknowledgments

The writers thank Markus Spiegl, Karl Kappl, Michael Wistuba, and Ronald Blab for providing the experimental data at the different observation scales. Financial support by the Christian Doppler Gesellschaft (Vienna, Austria) is gratefully acknowledged. The first writer is grateful for the financial support via the DOC-FFORTE program.

Appendix. Storage and Loss Modulus for the PL Model

For an oscillating strain history, with $\varepsilon(t)=\varepsilon_0 \exp(i\omega t)$ applied onto a uniaxially loaded specimen, the stress history is given when considering deviatoric deformations only by

$$\sigma(t) = \int_{-\infty}^{t} \mu(t-\tau)\frac{\partial \varepsilon(\tau)}{\partial \tau} d\tau = \varepsilon_0 i\omega \int_{-\infty}^{t} \mu(t-\tau)\exp(i\omega\tau) d\tau \tag{25}$$

Substituting τ in Eq. (25) by $\tau'=t-\tau$ and considering $\exp(i\omega\tau)=\exp(i\omega t)\exp(-i\omega\tau')$, Eq. (25) becomes

$$\sigma(t) = \varepsilon_0 \exp(i\omega t) i\omega \int_{0}^{\infty} \mu(\tau')\exp(-i\omega\tau') d\tau' \tag{26}$$

Considering $\varepsilon(t)=\varepsilon_0 \exp(i\omega t)$ in Eq. (26), the complex shear modulus μ^* (MPa), which is defined by $\mu^*=\sigma(t)/\varepsilon(t)$, is obtained as

$$\mu^* = i\omega \int_{0}^{\infty} \mu(\tau')\exp(-i\omega\tau') d\tau' \tag{27}$$

By comparison, the complex modulus is found to be equal to the Laplace-Carson transform of the shear relaxation modulus $\mu(t)$, reading

$$\mu^* = (i\omega)\mathcal{L}[\mu(\tau')]_{s=i\omega} = \mathcal{LC}[\mu(\tau')]_{p=i\omega} \tag{28}$$

In a similar manner, the complex creep compliance J^* is found as the Laplace-Carson transform of the creep compliance $J(t)$ as

$$J^* = (i\omega)\mathcal{L}[J(\tau')]_{s=i\omega} = \mathcal{LC}[J(\tau')]_{p=i\omega} \tag{29}$$

For the case of the PL model, with $J_{\mathrm{PL}}(t) = 1/\mu_0 + J_a(t/\bar{\tau})^k$, Eq. (29) yields

$$J^*_{\mathrm{PL}} = \frac{1}{\mu_0} + J_a(i\omega\bar{\tau})^{-k}\Gamma(1+k) \tag{30}$$

where $\Gamma(x)$ denotes the gamma function. Considering $\mu^* = 1/J^*$, the complex modulus for the PL model reads

$$\mu^*_{\mathrm{PL}} = \frac{1}{1/\mu_0 + J_a(i\omega\bar{\tau})^{-k}\Gamma[1+k]} \tag{31}$$

The storage modulus μ' and the loss modulus μ'', required in the course of parameter identification from cyclic experiments, are obtained as the real and imaginary parts, respectively, of μ^*, reading

$$\mu'_{\mathrm{PL}} = \frac{1}{D}\left[\frac{1}{\mu_0} + J_a(\omega\bar{\tau})^{-k}\Gamma(1+k)\cos\frac{k\pi}{2}\right]$$

$$\mu''_{\mathrm{PL}} = \frac{1}{D}\left[J_a(\omega\bar{\tau})^{-k}\Gamma(1+k)\sin\frac{k\pi}{2}\right] \tag{32}$$

with

$$D = \left(\frac{1}{\mu_0} + J_a(\omega\bar{\tau})^{-k}\Gamma(1+k)\cos\frac{k\pi}{2}\right)^2 + \left(J_a(\omega\bar{\tau})^{-k}\Gamma(1+k)\sin\frac{k\pi}{2}\right)^2 \tag{33}$$

Hereby, for the determination of μ' and μ'', $(i\omega\tau)^{-\alpha}$ in Eq. (31) is replaced by $(\omega\tau)^{-\alpha}[\cos(\alpha\pi/2) - i\sin(\alpha\pi/2)]$. Accordingly, μ^* takes the form $\mu^* = 1/(a+ib)$. The real and imaginary parts of μ^* are obtained from

$$\mu^* = \frac{1}{a+ib} = \frac{1}{1+ib}\frac{a-ib}{a-ib} = \frac{a-ib}{a^2+(-b)^2} = \frac{a-ib}{a^2+b^2} = \left[\frac{a}{a^2+b^2}\right] + i\left[\frac{-b}{a^2+b^2}\right] \tag{34}$$

giving

$$\mu' = \mathrm{Re}(\mu^*) = \frac{a}{a^2+b^2} \quad \text{and} \quad \mu'' = \mathrm{Im}(\mu^*) = i\frac{-b}{a^2+b^2} \tag{35}$$

Notation

The following symbols are used in this paper:

$\mathbf{A}$ = fourth-order localization tensor;
$\mathbf{A}_I$ = fourth-order localization tensor for the Ith inclusion;
b = width of BBR bitumen/mastic beam;
$\mathbf{C}_{\mathrm{eff}}$ = effective elastic material tensor of composite material;
c = parameter describing dependence of p on T;
$\mathbf{c}$ = elastic material tensor;
$\mathbf{c}_I$ = elastic material tensor of the Ith inclusion;
$\mathbf{c}_M$ = elastic material tensor of matrix;
$\mathbf{c}_r$ = elastic material tensor of rth material phase;
$\mathbf{E}$ = homogeneous strain tensor;
E_a = activation energy;
F = load applied in BBR experiments;
f_a = volume fraction of air voids;
f_{eff} = effective volume content;
f_f = volume fraction of filler;
f_I = volume fraction of inclusion;
f_M = volume fraction of matrix;
f_s = volume fraction of stone;
H = initial creep-compliance rate;
H_0 = value of H at reference temperature $\bar{T}$;
h = height of BBR bitumen/mastic beam;
$\mathbf{I}$ = fourth-order unity tensor;
J = creep compliance;
J_a = viscous part of the creep compliance at $t=\bar{\tau}$;
J_a = creep compliance of air;
J_b = creep compliance of bitumen;
J_{eff} = effective creep compliance of composite material;
J_f = creep compliance of filler;
J_I = creep compliance of the Ith inclusion;
J_M = creep compliance of matrix;
k = creep exponent;
k_b = bulk modulus of bitumen;
k_M = bulk modulus of matrix;
ℓ = length of BBR bitumen/mastic beam;
M = bending moment;
p = slope of creep-compliance rate in $\log dJ/dt$-$\log t$ diagram;
p_0 = value of p at reference temperature $\bar{T}$;
R = gas constant, with $R = 8.31$ J/mol/K;
$\mathbf{S}_I$ = fourth-order Eshelby tensor for the Ith inclusion;
T = temperature;
$\bar{T}$ = reference temperature;
t = time;
u = midspan deflection of BBR beam;
V = volume of RVE;
W = section modulus;
$\mathbf{x}$ = spatial coordinate vector;
β = quantity representing the Eshelby tensor in case of spherical inclusions;
ε = strain;
$\boldsymbol{\varepsilon}$ = local strain tensor;
$\boldsymbol{\varepsilon}_r$ = local strain tensor of rth material phase;
Γ = gamma function;
μ = shear modulus;
μ_{eff} = effective shear modulus of composite material;
μ_f = shear modulus of filler;
μ_I = shear modulus of the Ith inclusion;
μ_M = shear modulus of matrix;
μ_s = shear modulus of stone;
ρ_d = dry density at maximum compaction;
ρ_s = grain density;
$\boldsymbol{\Sigma}$ = homogeneous stress tensor;
$\boldsymbol{\sigma}$ = local stress tensor;
$\boldsymbol{\sigma}_r$ = local stress tensor of rth material phase;
σ = stress;
$\bar{\tau}$ = constant time parameter, with $\bar{\tau} = 1$ s;
φ = phase angle; and
ω = angular frequency.

References

Blab, R., et al. (2004). *Midterm Rep. Prepared for Christian Doppler Laboratory for Performance-Based Optimization of Flexible Pavements*, Vienna Univ. of Technology, Vienna, Austria.

DIN-18126. (1996). *Baugrund, Untersuchung von Bodenproben—Bestimmung der Dichte nichtbindiger Böden bei lockester und dichtester Lagerung [Soil, investigation and testing—Determination of density of granular soils for minimum and maximum compactness]*. Deutsches Institut für Normung e. V., Berlin (in German).

Ewers, J., and Heukelom, W. (1964). "Die Erhöhung der Viskosität von Bitumen durch die Zugabe von Füller [The increase of bitumen viscosity by the allowance of filler]." *Str. Autob.*, 2, 31–39.

Holl, A. (1971). *Bituminöse Straßen: Technologie und Bauweisen [Flexible pavements: Technology and design]*, Bauverlag, Wiesbaden, Germany (in German).

Huet, C. (1963). "Étude par une méthode d'impédance du comportement viscoélastique des matériaux hydrocarbonés [Study of the viscoelastic behavior of bituminous mixes by method of impedance]." Ph.D. thesis, Faculte des Sciences de Paris, Paris (in French).

Lackner, R. (2004). "Multiscale modeling as the basis for reliable predictions of the behavior of multi-composed materials." *Progress in computational structures technology*, B. Topping and C. Mota Soares, eds., Saxe-Coburg, Stirling, 153–187.

Mandel, J. (1966). *Méchanique des milieux continus [Mechanics of continuous media]*, Gautheir, Paris (in French).

Mori, T., and Tanaka, K. (1973). "Average stress in matrix and average elastic energy of materials with misfitting inclusions." *Acta Metall.*, 21, 571–574.

Pichler, C., and Lackner, R. (2009). "Upscaling of viscoelastic properties of highly-filled composites: Investigation of matrix-inclusion-type morphologies with power-law viscoelastic material response." *Composites Science and Technology*, 69, 2410–2420.

Pichler, C., Lackner, R., and Aigner, E. (2009). "Generalized self-consistent scheme for upscaling of viscoelastic properties of highly-filled matrix-inclusion composites—Application in the context of multiscale modeling of bituminous mixtures." *Fuel.*, submitted.

Olard, F. (2003). "Comportement thermoméchanique des enrobés bitumineux à basses températures. Relations entre les propriétés du liant et de l'enrobé [Thermomechanical behavior of bituminous mixtures at low temperatures. Relations between characteristics of binder and properties of bituminous mixtures]." Ph.D. thesis, Ecole Nationale des TPE, Lyon.

ÖNORM-EN-1097-4. (1999). *Prüfverfahren für mechanische und physikalische Eigenschaften von Gesteinskörnungen—Teil 4: Bestimmung des Hohlraumgehaltes an trocken verdichtetem Füller [Tests for mechanical and physical properties of aggregates—Part 4: Determination of the void content of dry compacted filler]*, Österreichisches Normungsinstitut, Vienna, Austria (in German).

ÖNORM-EN-12697-26. (2004). *Asphalt—Prüfverfahren für Heißasphalt—Teil 26: Steifigkeit [Bituminous mixtures—Test methods for hot-mix asphalt—Part 26: Stiffness]*, Österreichisches Normungsinstitut, Vienna, Austria (in German).

Sayegh, G. (1965). "Contribution à l'étude des propriétés viscoélastique des bitumes purs at des bétons bitumineux." Ph.D. thesis, Sorbonne, Paris (in French).

SHRP-A-370. (1994). *Binder characterization and evaluation. Volume 4: Test methods*, Strategic Highway Research Program, National Research Council, Washington, D.C.

Stehfest, H. (1970). "Algoritm 368: Numerical inversion of Laplace transforms." *Commun. ACM*, 13, 47–49.